This is a postprint version of the following published document:

Ogata, D., Newman, D. E., & Sánchez, R. (2017). Transport dynamics of self-consistent, near-marginal drift-wave turbulence. II. Characterization of transport by means of passive scalars. *In Physics of Plasmas, 24*(7), 072310

Transport dynamics of self-consistent, near-marginal drift-wave turbulence. Part I. Investigation of the ability of external flows to tune the non-diffusive dynamics.

D. Ogata,[1, a)] D. E. Newman,[1] and R. Sánchez[2]

[1)] *Department of Physics, University of Alaska, Fairbanks, AK 99775-5920, USA*

[2)] *Departamento de Física, Universidad Carlos III, Leganés 28911, Madrid, SPAIN*

The reduction of turbulent transport across sheared flow regions has been known for a long time in magnetically confined toroidal plasmas. However details of the dynamics are still unclear, in particular in what refers to the changes caused by the flow on the nature of radial transport itself. In a companion paper, we have shown in a simplified model of drift wave turbulence that, when the background profile is allowed to evolve self-consistently with fluctuations, a variety of transport regimes ranging from superdiffusive to subdiffusive open up depending on the properties of the underlying turbulence [D. Ogata et al, *Physics of Plasmas* (submitted, 2016)]. **In this paper, we show that externally applied sheared flows can, under the proper conditions, cause the transport dynamics to be diffusive or subdiffusive.**

I. INTRODUCTION

Radial transport in magnetically confined fusion plasmas has been an area of active investigation for many years. Methods for regulating radial turbulent transport could provide a balance between improved confinement and ash removal. There is a large body of work with experiments on various devices and plasmas simulations of different kinds have shown that sheared flows tend to suppress transport across the flow[1–3]. In fact, it is this type of transport reduction that is believed to be responsible for the access to improved confinement in current tokamak configurations, where a large radially-sheared poloidal flow appears at the so-called pedestal region near the plasma edge.

However, there are still many aspects of the process by which sheared flows reduce transport across them that remain unclear. Traditionally, it has been thought that the main action of a sheared flow on turbulent fluctuations is to reduce its size perpendicular to the direction of the flow, which leads to a reduced effective transport coefficient in that direction. However, recent studies with ion-temperature-gradient (ITG) gyrokinetic turbulence in a tokamak geometry have shown that, if the radial shear in the poloidal flow is sufficiently large, the intimate nature of the transport process changes, becoming subdiffusive instead of just diffusive[4,5]. An important limitation of these simulations, though, was that they were carried out using the commonly used fixed-gradient setup, in which the background profiles are kept fixed while turbulence is evolved. Background evolution is however important in this context, particularly if the background profiles remain close to near-marginal conditions, when the separation of timescales between turbulence and profile evolution narrows. In near-marginal conditions, coherent

relaxations of the profile can propagate both down and up the background gradients (the so-called "avalanches") leading to superdiffusive transport[6,7]. There are theoretical reasons to expect that sheared flows should have an important impact on these coherent relaxations[8]. Regretfully, the kind of flux-driven numerical plasma simulations needed to explore these questions, in which background profiles, turbulence and flows should be advanced simultaneously and self-consistently, remain very expensive numerically, specially in a gyrokinetic context. Thus, studies on the nature of radial transport in these conditions, although relevant for next-step tokamaks such as ITER, have remained scarce[9].

In order to shed some light onto this matter, we have constructed a simpler two-dimensional flux-driven model, based on drift-wave turbulence in a bi-periodic slab geometry, that includes the simultaneous, self-consistent evolution of profiles, turbulence and flows, whose relative simplicity allows for sufficiently long simulations. In a companion paper[10], we characterized the transport dynamics of the model that may exhibit a whole range of transport dynamics, going from superdiffusive to subdiffusive simply by varying the parameters that define it. The mechanisms responsible for this behavior were easily identified, being related to the ability of the turbulence-induced transport can relax supramarginal profiles back below the local thresholds, the degree of competition offered by other transport mechanisms and the importance of the flows self-generated by the turbulence. In this paper, we explore instead the possibilities of control offered by externally applied flows in order to tune at will the desired transport dynamics of the system.

With that idea in mind, we have included an external poloidal flow within the simple drift-wave model as is described in Sec. II. The changes induced in the transport dynamics by the external flows are monitored by means of a characteristic transport exponent, H, that is introduced in Sec. III, as well as the technique to measure it using tracer particles[11]. The next sections discuss the

---

a)Electronic mail: dogata@alaska.edu

results obtained with the model. First, in order to connect the results with previous work, Sec. IV presents the modifications of the characteristics of transport induced by the externally imposed flows in the case in which turbulence is evolved with a fixed-profile. Then, in Sec. V, the same cases are re-analyzed but using instead a flux-driven setup in which proper background evolution is enabled. Finally, Sec. VI summarizes the main results of the work.

II. DRIFT-WAVE TURBULENCE MODEL

The model that will be used in this paper is based on a collisional drift-wave model for plasma turbulence[12]. The model is formulated in a bi-periodic slab geometry that assumes a constant perpendicular magnetic field. The spatial domain is a periodic square in the xy plane. The coordinate $x \in [0,1]$ mimics the radial direction (in a magnetic toroidal configuration), while the coordinate $y \in [0,1]$ emulates the poloidal direction. The governing evolution equations for this electrostatic model are three:

$$\frac{d}{dt}\left[\left(1 - \sqrt{\epsilon} - \rho_s^2 \nabla_\perp^2\right)\phi\right] = -\left(1 - \sqrt{\epsilon}\,\xi\right)C_s\rho_s\Psi\left(n,\phi,P\right)$$
$$+\nu\sqrt{\epsilon}\left(n-\phi\right) - \mu\rho_s^2\nabla_\perp^4\phi$$
$$\frac{dn}{dt} = -\xi C_s\rho_s\Psi\left(n,\phi,P\right) \qquad (1)$$
$$+\nu_{eff}\left(\phi - n\right)$$
$$\frac{dP}{dt} = S + D_P\nabla_\perp^2 P$$

where n is the fluctuating density, ϕ is the fluctuating potential, and P is the background profile. **The advective derivative is defined with an external flow $\boldsymbol{u}_0$ as $d/dt = \partial_t + (\boldsymbol{u}_0 + \boldsymbol{u})\cdot\boldsymbol{\nabla}$.** The first two equations are essentially the same as those of the standard DTEM model[12,13], except in that they include an additional dependence on the background profile P via the nonlinear function $\Psi(n,\phi,P)$, that we discuss later. The third equation, on the other hand, gives the evolution of the background profile P in the presence of an external drive S. The definitions and meanings of the coefficients appearing in the model are also quite standard: $\rho_s = (k_B T_e/eB)/C_s$ is the ion gyroradius, $C_s = \sqrt{k_B T_e/m_i}$ is the ion sound speed, $\xi = (1 + \alpha\eta_e)$ where $\eta_e = \partial(\ln T)/\partial(\ln n) = 2$ and $\alpha = 3/2$ for the instability criterion for destabilization of DTEM modes by electron collision[12], ϵ is the inverse aspect-ratio that gives the trapped electron fraction, μ is the viscosity coefficient, ν is the electron collisional relaxation due to trapping and detrapping, and $\nu_{eff} = \nu/\epsilon$. The trapped electron fraction ϵ affects the instability of the drift-waves in relations to the regime of collisionality ν[12].

The adiabatic limit of the model is achieved when $\nu \to \infty$, in which the relationship between n and ϕ reduces to the "$i\delta_k$" approximation[14] that specifies the nonadiabatic trapped electron response. The turbulence

evolution is then described through a single equation where n responds to ϕ nonlocally[12,15,16]. Mid-sized tokamaks operate in this high collisional regime where the ion detrapping occurs before banana orbits are formed[12], which then allows for a phase shift between n and ϕ. The coupling term $n - \phi$ is defined to evolve with the $k_y = 0$ modes unlike models with zonal flows[2] such as the modified Hasegawa-Wakatani model[17]. **This means that the adiabatic response for $k_y = 0$ is not set to zero. According to previous works on zonal flows on a fixed-gradient setup, the elimination of the $k_y = 0$ modes allow a more efficient formation of zonal flows[17–19]. Comparisons between transport due to restricted and self-consistent zonal flows have been explored under fixed-gradient setup[4,5], but this has not been explored in this model.** The hydrodynamic limit occurs when $\nu \to 0$, which decouples the n from the ϕ evolution equation. The equation for ϕ resembles a 2D neutral fluid equation while the n equation becomes that of a passive scalar. Large tokamaks are in this low collisional regime[12].

In the evolution of the background profile, P, S is the source term and D_P is a classical diffusion coefficient. It must be noted that the inclusion of an evolution equation for P makes the simulation flux-driven, which means that the local flux $\boldsymbol{\Gamma}_P = \boldsymbol{u}P$, where $\boldsymbol{u} = C_s\rho_s\hat{\boldsymbol{z}}\times\boldsymbol{\nabla}\phi$, adapts itself to balance the incoming net drive. This drive is constructed as the sum of a Gaussian of a fixed-width, $G_w(x)$, and prescribed positive height, S_0, located at $x_{\text{source}} = 0.25$ and another Gaussian equal in magnitude but of reversed sign at $x_{\text{sink}} = 0.75$:

$$S(x) = S_0\left[G_w(x - x_{\text{source}}) - G_w(x - x_{\text{sink}})\right]. \qquad (2)$$

S_0 represents the injection rate. It is set to $S_0 = 5$ in all simulations in this paper.

The model permits the self-generation of flows via the Reynolds stress term, that expresses itself in the form of two non-linearities, but requires turbulence to be sufficiently inhomogeneous and anisotropic for significant flow generation[1,20]. The first nonlinearity is the $E \times B$ nonlinearity, that appears in the n evolution equation and represents the advection on the fluctuating density n, given by the term $\boldsymbol{u}\cdot\boldsymbol{\nabla}_\perp n = C_s\rho_s\hat{\boldsymbol{z}}\times\boldsymbol{\nabla}_\perp\phi\cdot\boldsymbol{\nabla}_\perp n$. The second is the polarization drift nonlinearity, that arises from the advection on the vorticity, $\nabla_\perp^2\phi$, and is given by the term $\boldsymbol{u}\cdot\boldsymbol{\nabla}_\perp\left(\nabla_\perp^2\phi\right) = C_s\rho_s^3\hat{\boldsymbol{z}}\times\boldsymbol{\nabla}_\perp\phi\cdot\boldsymbol{\nabla}_\perp\left(\nabla_\perp^2\phi\right)$. The interplay of these two nonlinearities has been studied extensively in simulations that, in contrast to the ones performed here, assumed a fixed background gradient[13,15,16,21]. The polarization drift nonlinearity is found to be dominant at large wave numbers due to difference in the k^2 coming from the vorticity term.

The self-generation of flows can be directly driven by the $E \times B$ nonlinearity. To the first approximation, it can be seen by noting that the poloidal velocity is $u_y = \partial_x\phi$ and performing the flux-average on the ϕ equation in Eq. 1, which

gives

$$\left(1 - \sqrt{\epsilon}\right) \frac{\partial}{\partial t} \langle u_y \rangle_y - \rho_s^2 \frac{\partial}{\partial x} \left\langle \frac{\partial}{\partial x} \left(u_x \nabla^2 \phi\right) \right\rangle_y =$$

$$\nu \sqrt{\epsilon} \left(\frac{\partial}{\partial x} \langle n \rangle_y - \langle u_y \rangle_y\right) - \mu \rho_s^2 \nabla^4 \langle u_y \rangle_y . \qquad (3)$$

The second term in the left hand side represents the advection on the vorticity, which can provide the asymmetry necessary to generate sheared flows. Hence, the model inherently generates sheared flows that are amplified under the flux-driven setup. There is no free parameter in this model that directly regulates the self-generated flows.

In addition to self-generated sheared flows, the possibility of having externally-imposed flows has also been introduced in the model through the advective derivative operator, $d/dt = \partial_t + (\boldsymbol{u}_0 + \boldsymbol{u}) \cdot \boldsymbol{\nabla}$. The external flow is defined as $\boldsymbol{u}_0 = C_s \rho_s \hat{\boldsymbol{z}} \times \boldsymbol{\nabla} \phi_0$, being ϕ_0 an externally defined electrostatic potential with a radial profile given by $\phi_0 = \Phi_0 \cos\left(2\pi x\right)$. In this way, the velocity profile is $\boldsymbol{u}_{\text{ext}} \sim \Phi_0 \sin\left(2\pi x\right) \hat{\boldsymbol{y}}$, reaching its maximum shear at $x = 0.5$. The external flow remains incompressible since $\boldsymbol{\nabla} \cdot \boldsymbol{u}_0 = 0$. It must be noted that the external electrostatic profile ϕ_0 is not included in the **nonadiabatic collisional detrapping**; therefore, ϕ_0 is not added to the term proportional to the difference $n - \phi$ in the evolution equation for ϕ.

We discuss next the nonlinear function $\Psi\left(n, \phi, P\right)$, that includes the threshold condition that introduces the possibility of profiles being near-marginal. The term is defined as:

$$\Psi\left(n, \phi, P\right) = f_d \left[g\left(L_{\langle P \rangle_y, x}^{-1}\right) L_{\langle P \rangle_y, x}^{-1} \left(-\frac{\partial \phi}{\partial y}\right)\right]$$

$$+ \left(1 - f_d\right) \left[g\left(L_{P,y}^{-1}\right) L_{P,y}^{-1} \frac{\partial \phi}{\partial x} + g\left(L_{P,x}^{-1}\right) L_{P,x}^{-1} \frac{\partial \phi}{\partial y}\right] (4)$$

Its meaning is explained in depth in the companion paper[10], but we repeat the fundamentals here for clarity. The main ingredient is the function $g(L_{s,z}^{-1})$, defined as:

$$g(L_{s,z}^{-1}) = \frac{1}{2} \left[2 + \tanh\left(\kappa\left(L_{s,z}^{-1} - L_{c,s,z}^{-1}\right)\right) - \right.$$
$$\left. - \tanh\left(\kappa\left(L_{s,z}^{-1} + L_{c,s,z}^{-1}\right)\right)\right] \qquad (5)$$

where $L_{c,s,z}^{-1}$ is a prescribed critical value for the gradient of field s in the z direction, $\kappa[= 20]$ prescribes the steepness of the hyperbolic tangent function, and $L_{s,z}^{-1} := \partial_z s/s_0$ is the local gradient (s_0 is an arbitrary normalization constant). The main point is that $g(L_{s,z})$ essentially vanishes if $L_{s,z}^{-1} < L_{c,s,z}^{-1}$, and is equal to one if $L_{s,z}^{-1} > L_{c,s,z}^{-1}$, thus introducing a threshold for the excitation of turbulence in the problem. It is the combination of the presence of this term and the flux-driven setup that permits the system to stay near-marginality if the proper conditions are met. Eq. 4 includes however several possible thresholds, weighted by the $f_d \in (0, 1)$

factor. The first line introduces a threshold on the radial gradient of the poloidally averaged background profile; the second line, two thresholds, one on the local radial gradient of the background profile, another on the local poloidal gradient. This combination has been introduced to make possible the study of the importance of a partial parallel equilibration across magnetic surfaces[10], which might be an issue in tokamaks, particularly closer to the edge where dynamics are more collisional, or in the neighborhood of rational surfaces. Indeed, if $f_d = 1$, it is assumed that any inhomogeneities along y are quickly equilibrated, and that only the poloidally-averaged background profile (denoted by $\langle \cdot \rangle_y$) matters in terms of providing the turbulence with free energy. On the other hand, $f_d = 0$ means that there is no parallel equilibration whatsoever, and only local gradients matter.

Fixed background gradient scenarios can also be easily run in this model. One just needs to solve Eq. 1 with $dP/dt = 0$, set $f_d = 1$, impose $g\left(L_{\langle P \rangle_y, x}^{-1}\right) = 1.0$ and, finally, prescribe a fixed value for the background gradient, $L_{\langle P \rangle_y, x}^{-1} = \partial_x \langle P \rangle_y / P_0$. With these choices, the nonlinear function reduces to $\Psi\left(n, \phi, P\right) = L_{\langle P \rangle_y, x}^{-1} \partial_y \phi$ such that $C_s \rho_s \Psi\left(n, \phi, P\right) = V_D \partial_y \phi$ where $V_D = C_s \rho_s / L_{\langle P \rangle_y, x} = \left(k_B T_e / eB\right) L_{\langle P \rangle_y, x}^{-1}$, a common form for the diamagnetic drift. In this case, assuming a constant external flow $\boldsymbol{u}_0 = U_0 \hat{\boldsymbol{x}}$ yields a linear dispersion for perturbations of the form $\propto \exp\left[i\left(k_x x + k_y y\right) - i\omega t\right]$ given by:

$$0 = \left(\omega'\right)^2 - \omega' \left[\left(1 - \sqrt{\epsilon}\xi\right)\omega_* - i\nu_{eff}\zeta\right] - i\nu_{eff}\omega_* \quad (6)$$

where $k^2 = k_x^2 + k_y^2$, the frequency shift $\omega' = \omega - U_0 k_x$, the electron diamagnetic drift frequency $\omega_* = k_y V_D / \left(1 - \sqrt{\epsilon} + \rho_s^2 k^2\right)$, and the ϵ dependent contribution of the resistive coupling $\zeta = \left(1 + \rho_s^2 k^2\right) / \left(1 - \sqrt{\epsilon} + \rho_s^2 k^2\right)$. This linear dispersion relation, except for the U_0-shift, is identical to that of the standard DTEM model[16], as it should be.

We conclude this section by providing some details about the numerical scheme used to solve Eq. 1. The spatial domain considered is a doubly-periodic grid of 256×256 nodes in the Fourier space spanned by k_x and k_y. The scheme used is a standard spectral one, properly modified to avoid any aliasing problems, that uses the pseudo-spectral method to deal with nonlinearities. The temporal integration is done implicitly, using a scaled preconditioned Generalized Minimal Residual (GMRES) solver that combines well-established integration schemes[22]. Parallelization is achieved by using MPI and by taking advantage of parallel Fast Fourier Transform (FFT) routines, as well as other parallel numerical integration routines. All simulations have been initialized with random phases for all Fourier harmonics, and they have been advanced in time until a suitable quasi-steady state, with approximate balance between drive and losses, is established.

III. TRANSPORT CHARACTERIZATION

Removed the introduction with Fick's law. There are many ways to define the characterize the nature of transport in a system[23,24]. By extension of standard diffusion, some authors define nondiffusive transport as any situation in which the evolution of P in Eq. 1 follows instead a transport equation of the form:

$$\frac{\partial^\beta P}{\partial t^\beta} = \chi_{\alpha,\beta} \frac{\partial^\alpha P}{\partial |x|^\alpha}. \qquad (7)$$

for $x \in \mathbb{R}$ and $t \in \mathbb{R}^+$ where $\chi_{\alpha,\beta}$ is a scaling constant. The exponent ranges are $\alpha \in (0,2)$ and $\beta \in (0,1)$. This equation is a generalization of the more usual classical diffusive equation, where $\beta = 1$ and $\alpha = 2$, based on fractional derivatives. These fractional operators provide a smooth interpolation in between integer derivatives[25]. Thus, the type of transport that can be captured by Eq. 7 may be non-local (if $0 < \alpha < 2$) and non-Markovian (if $0 < \beta < 1$). The exponent of interest to us, however, is $H := \beta/\alpha$. Transport is called superdiffusive if $H > 1/2$, diffusive if $H = 1/2$ and subdiffusive if $H < 1/2$. The reason for this name is that any population of particles, whose transport is governed by Eq. 7 and that are initially localized in x, will spread faster (if $H > 1/2$) or slower (if $H < 1/2$) than its diffusive counterpart.

The transport exponent H can be estimated in many ways. A very useful way is to take advantage of the fact that the transport equation like Eq. 7 can be derived from "microscopic considerations" that relate to the distribution of particle motion[23,24,26]. It can also be derived as the long-term, long-distance limit of the generalized Langevin equation[11,27]

$$x(t) = x_0 +$$
$$+ \frac{1}{\Gamma(H - 1/\alpha + 1)} \int_0^t (t-t')^{H-1/\alpha} \xi_\alpha(t') dt', \qquad (8)$$

that assumes a non-random forcing with symmetric α-Lévy statistics and a correlation in time characterized with a Hurst exponent $H \in (0,1)$[28]. H is also the self-similarity exponent of the trajectory, $x(t)$. In that case, the resulting temporal exponent in the transport equation Eq. 7 is given by $\beta = \alpha H$.

The connections of Eq. 7 with these "microscopic formulations" can be exploited to come up with methods to determine the fractional exponents in practical situations, and thus to provide ways to characterize the nature of transport. Among the different methods available, in this paper we will focus on one that exploits the connection with Eq. 8 to determine H. It just requires following the trajectories of massless tracer particles as they are advected by the turbulence. That is, to integrate in time their velocity, that is given by,

$$\dot{\boldsymbol{R}}(t) = \boldsymbol{E} \times \boldsymbol{B}/B^2 = C_s \rho_s \hat{\boldsymbol{z}} \times \boldsymbol{\nabla}_\perp \phi, \quad \boldsymbol{R}(t_0) = \boldsymbol{r_0}, (9)$$

since the advection in our model is done by the turbulent fluctuating $E \times B$ velocity. **Removed discussion of CTRW.**

Removed the definition of R/S. Since H represents the self-similarity exponent of the trajectory described by Eq. 8, it must also happen that it is the correlation (or Hurst) exponent of its derivative, or time series of the increments of the process. Or, in discrete form, H also represents the velocity series along the Lagrangian trajectory. The method we have chosen to determine this correlation exponent is the well-known R/S technique, that has been reliably used for more than sixty years[28]. It then happens that, if the signal is correlated with Hurst exponent H (and therefore, its integrated path is self-similar with the same exponent), one finds that,

$$(R/S)_n \propto n^H, \qquad (10)$$

from which the exponent is readily obtained. It is fair to say that the R/S method has been criticized in the literature because it tends to somewhat overestimate exponents (for instance, R/S tends to yield $H \sim 0.55$ for random signals instead of 0.5), but it is extremely resilient to both noise and periodic perturbations[29], which is why it is our method of choice. It is also worth to note that the statistics of the determination of H are greatly improved by averaging the rescaled range for time n over all non-overlapping segments of size n in which the full time series can be broken, procedure that we have extensively used in this work.

IV. TRANSPORT CHARACTERISTICS OF CASES RUN WITH A FIXED BACKGROUND PROFILE IN THE PRESENCE OF AN EXTERNALLY-IMPOSED SHEARED FLOW

An externally-imposed sheared flow can act as a decorrelation mechanism when the shear strain rate produced by the external sheared flow is greater than the eddy turnover rate[1]. The added decorrelation acts to inhibit the transport across the sheared region, while enhancing advection in the flow direction. This inhibited transport has been recently shown to exhibit subdiffusive features across the flow, and to behave superdiffusively along the flow in recent gyrokinetic simulations with fixed background gradients[4,5]. **Removed the discussion about shear strain rate.**

In order to better understand the action of an external flow in situations in which profile turbulent modification and flow generation happen simultaneously, self-consistently and in near-marginal conditions, we have started our analysis by looking first at the simpler (and more traditional) case in which profile modification is disabled. To do that, we have run the DTEM model in a fixed-background-mode. That is, we set $dP/dt = 0$, $f_d = 1$, impose $g\left(L_{\langle P \rangle_y, x}^{-1}\right) = 1$ and choose a value $L_{\langle P \rangle_y, x}^{-1} = 0.5$, so that a constant, fixed gradient provides free energy for the turbulence. These choices also bring us close to the majority of previous work by many authors, which should allow for a more meaningful com-

parison when we allow profile modification to happen in the next section.

In drift-wave turbulence, however, one needs to be careful. An additional mechanism exists, independent of the presence of self-generated sheared flows, that can yield subdiffusive radial transport, and superdiffusive poloidal transport. It emerges after the nonlinearly saturated state has been achieved due to the linear (poloidal) diamagnetic drift[30–34]. Hence, in order to demonstrate any subdiffusive influence of an externally-imposed flow, the shear strain rate defined through Φ_0 must overcome that from the diamagnetic wave term. That is, the shear strain rate imposed by the external flow must effectively decorrelate the eddies faster than the effect from the diamagnetic drift. We have made sure that this is the case by modifying some of the parameters that define the DTEM model, while keeping $\Phi_0 = 0$, until the resulting transport has diffusive features in all directions, implying that the action of the diamagnetic wave is negligible. The two parameters that have been varied in this search are ν and ϵ, that respectively represent the electron collisionality and the trapped electron fraction. **Removed figure and discussion of the parameter scan of ν and ϵ.**

From the results from the tracer analysis, it is apparent that, consistently with previous observations[30–34], radial subdiffusion (and superdiffusive poloidal motion) depends quite strongly on the value of ν. At the largest values of ν we have explored, the radial subdiffusive signature becomes quite strong. This subdiffusive signature, as previously said, comes primarily from the temporal decorrelation from the diamagnetic drift instead of from the action of any self-consistently generated sheared flow. **At smaller values of ν close to the largest diamagnetic drift frequency $\omega_* \sim 0.5$, transport becomes more diffusive.** From these results, we decided to move into a parameter regime in which the electron collisional relaxation is **on the order of the maximum diamagnetic drift frequency $\nu \to \omega_*$**, and the trapped electron fraction becomes large $\epsilon \to 1$ in order to isolate and make easier the analysis of the effect of external flows on transport in the model. The disadvantage of this parameter regime, on the other hand, is that the linear growth rate becomes larger due to the quadratic nature of the eigen-frequencies from Eq. 6. This means that the turbulence becomes more susceptible to instabilities, particularly those of the Kelvin-Helmholtz type[35].

Next, we proceeded to add external flows of varying amplitude Φ_0 to simulations run in the regime we just chose. The resulting vorticity fields, $\nabla_\perp^2 \phi$ are shown in Fig 1 for some representative cases. It can be appreciated that the maximum value of Φ_0 that can be used is indeed limited by the onset of Kelvin-Helmholtz instabilities, as expected. **Due to the periodic boundary conditions, the vortices appear at $x = n/2$ where $n = 0, 1, 2, \ldots$. However, the vortices are staggered since they are composed of staggered chains of convection cells and unstable to rotat-**
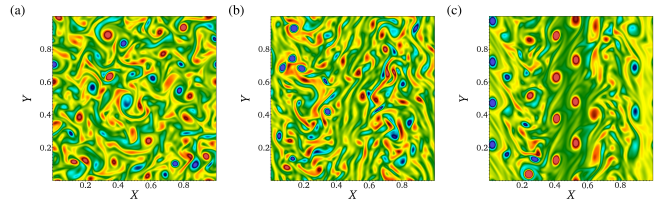

FIG. 1. Vorticity field $\nabla^2 \phi$ in real space for three values of Φ_0: (a) $\Phi_0 = 0$, (b) $\Phi_0 = 1.5$, and (c) $\Phi_0 = 3$ in the regime in which the linear wave contribution is weak. Transport is diffusive in the absence of external flow (a). Elongation in the poloidal direction becomes prominent with larger flow amplitude $\Phi_0 = 1.5$ (b). A Kelvin-Helmholtz instability occurs near the regions with largest shear at large enough external flow amplitude $\Phi_0 = 3$ (c).

ing and tilting[36,37]. In this work, the vortices move in the x-direction depending on the sign and trigger turbulence when vortices of different sign interact. This can be seen at $x \sim 0.25$ and $x \sim 0.75$ in Fig. 1 (c). It has also been shown in a previous work on a fixed-gradient setup that Kelvin-Helmholtz instability reintroduces turbulence when zonal flows are amplified[17]. Instead of zonal flows, an external sheared flow is the source of free energy for the Kelvin-Helmholtz instability. As an illustration of the tracer analysis done, Fig. 2 shows a few rescaled ranges for the series of the x (or y) component of the tracer Lagrangian velocity. Two distinct regions are clearly visible. The first one, for timescales smaller than $\tau \Omega_i \sim 1$ corresponds to the self-correlation of turbulence, and are of no interest for the determination of the long-term properties of transport. The second region, for $\tau \Omega_i \gg 1$ is seen to scale as τ^H, thus defining the Hurst exponent. The transition timescale between these regions is seen to move to smaller values for larger Φ_0, though, which points to the reduction in the autocorrelation time of the turbulence as the shear strain time imposed by the external flow increases. At the larger timescales, it is clearly seen that radial subdiffusion is enhanced by the presence of the external flow. Radial transport becomes more subdiffusive with the stronger shear. In the poloidal direction, the reverse behavior is observed. The level of superdiffusion increases as the shear becomes stronger. In fact, the value of the Hurst exponent exceeds even the upper limit of 1, which we think is related to the presence of long-lived eddies that then allows the signal to be non-stationary.

We have collected the Hurst exponents obtained from all simulations in Fig. 3 as a function of the shear flow strength. As advertised, it is clear that radial transport can be forced to be more subdiffusive by means of externally applied flows with larger shear values; at the same time, poloidal transport becomes more superdiffusive. The possibility of controlling the dynamics ends, however, when the stability of the external flow is broken by the onset of Kelvin-Helmholtz instabilities at the
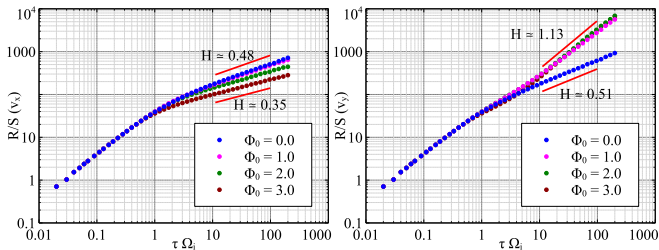
FIG. 2. Transport exponents with varying external flow amplitude Φ_0 on a fixed gradient setup show slight subdiffusion in the cross-flow direction but superdiffusion in the poloidal direction.
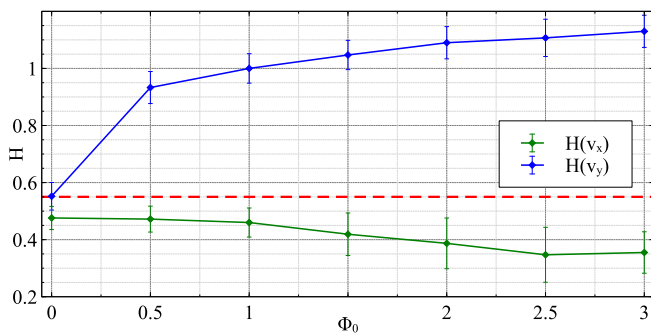

FIG. 3. Hurst parameters with varying external flow amplitude on a fixed gradient show subdiffusion in the cross-flow direction but strongly superdiffusion in the poloidal direction. The radial subdiffusive transport signature saturates at $H \sim 0.35$ due to the onset of a shear-driven instability.

positions of maximum flow shear. It is interesting to note that, in the case with fixed-gradients just examined, the value of H for radial transport (before any instability of the flow kicks in) saturates at around $H \sim 0.35$. This value is interestingly similar to the value obtained in pure Hasegawa-Wakatani models with self-consistent zonal flows[18]. This similarity points to the structure of the flow, and not the self-consistent interaction with the turbulence, as the more important factor in setting the value of the transport exponent H, at least in fixed-gradient simulations, as previously hinted at elsewhere[5].

V. TRANSPORT CHARACTERISTICS OF CASES RUN WITH PROFILE EVOLUTION IN THE PRESENCE OF AN EXTERNALLY-IMPOSED SHEARED FLOW

In this section, we proceed to explore the possibility of controlling the transport dynamics by means of externally-imposed sheared flows in the more realistic case in which a self-consistently evolving flux-driven profile replaces the fixed gradient used in the previous section. We have chosen as the base case with parameters $f_d = 0$ and $L_{c,P,x}^{-1} = 1$, so that a threshold local gradient exists in the radial direction. The source is chosen so that, in the case with no externally-imposed flows,

radial transport is superdiffusive and poloidal transport subdiffusive. **Again, the poloidal self-generated flows arising from the asymmetry in the Reynolds stress (Eq. 3) are only restricted by the choice of $L_{c,P,x}^{-1}$, which corresponds to the case when radial relaxation events dominate over the self-generated flows. This case is then used as the base case in order to investigate the effect of an external poloidal sheared flow on the radial transport.**
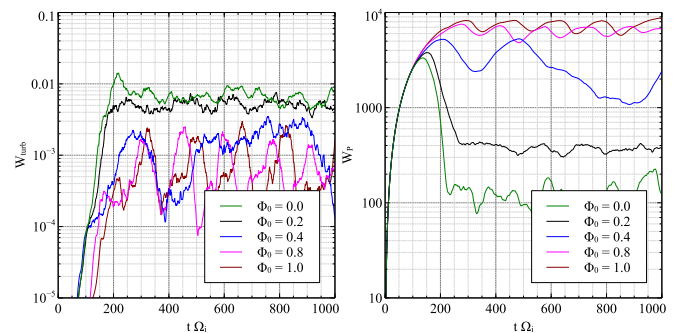

FIG. 4. Proxies for total energy W_{turb} (left) and W_P (right) reach quasi steady-states when the local turbulence balances the sources. Radial relaxations are inhibited with increasing Φ_0, which is reflected by the increase in $\langle W_P \rangle$. However, the turbulence decreases with increasing Φ_0. For large enough flow amplitude, flow-driven instabilities induce relaxations in W_P, also reflected as oscillations in W_{turb}.

In order to better quantify what is going on, we will use several proxy functions. In particular, we monitor $W_P \propto \int_0^1 |P|^2 \, dxdy$ and $W_{\text{turb}} \propto \int_0^1 |n|^2 + |\phi|^2 \, dxdy$. The first one represents the energy stored in the background; the second, the energy in the turbulence. In addition, we use $\delta W_{\text{turb}}/\langle W_{\text{turb}} \rangle_t$ and $\delta W_P/\langle W_P \rangle_t$ where $(\delta W_{\text{turb}})^2 = \left\langle (W_{\text{turb}} - \langle W_{\text{turb}} \rangle_t)^2 \right\rangle_t$ and $(\delta W_P)^2 = \left\langle (W_P - \langle W_P \rangle_t)^2 \right\rangle_t$ to respectively measure the burstiness (or activity) of the turbulence and of the profile modification processes. Here, $\langle \cdot \rangle_s$ means average over s. Typically, an steady-state means that both $W_P \sim$ constant and $W_{\text{turb}} \sim$ constant. In fixed-gradient simulations, $\delta W_P/\langle W_P \rangle_t = 0$, whilst the value of $\delta W_{\text{turb}}/\langle W_{\text{turb}} \rangle_t$ increases with the importance of turbulence-induced transport. In simulations where profiles are evolved, $\delta W_P/\langle W_P \rangle_t > 0$, being small in cases in which there is scarce profile modification (for instance, in supramarginal cases where profile stay well above threshold everywhere), and large when profile modification is intense (as in near-marginal regimes).

Fig. 4 shows the time traces of some of these functions for several flux-driven simulations with externally-applied sheared flows of varying amplitude. As it is easily seen, the steady state is reached for times $t\Omega_i > 200 - 300$. Several other conclusions can be drawn from these traces. First, the saturated value of W_{turb} decreases with a non-zero Φ_0, which reflects the turbulence sup-
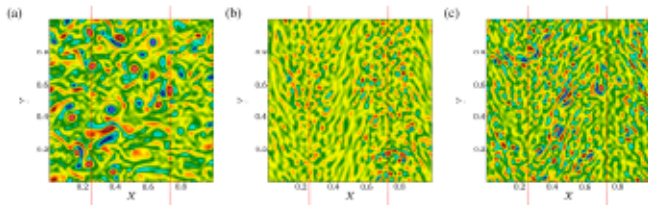
FIG. 5. Vorticity $\nabla^2\phi$ for three values of Φ_0 are shown: (a) $\Phi_0 = 0.0$, (b) $\Phi_0 = 0.6$, and (c) $\Phi_0 = 1.0$. Radially elongated structures corresponding to radial relaxations are more prominent for $\Phi_0 = 0.0$ in (a) than when the external flow produces a shearing effect in (b) for $\Phi_0 = 0.6$. Turbulence suppression is also prominent in (b). At a larger $\Phi_0 = 1.0$, individual eddies return in (c). Dashed red lines denote the source at $x_{source} = 0.25$ and the sink at $x_{sink} = 0.75$.
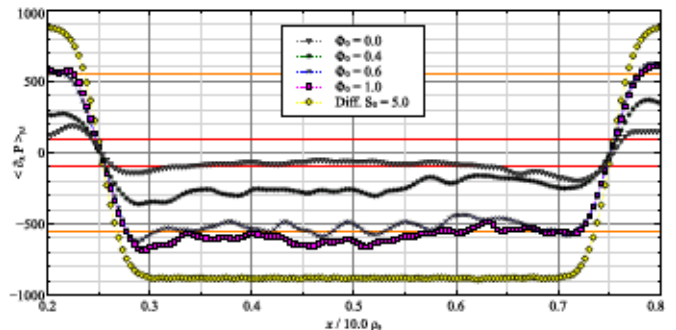

FIG. 6. Time and poloidal averaged background gradient profiles for varying amplitudes of the externally-imposed radially-sheared poloidal flow. Red lines correspond to the critical gradient parameter used, $L_{c,P,x}^{1} = 1$. Orange lines denote the approximate saturated gradient established at sufficiently large external flows ($\Phi_0 > 0.6$) around $L_{P,x}^{1} = 5.5$. The source is located at $x_{source} = 0.25$, and the sink is at $x_{sink} = 0.75$

pression carried out by the externally-driven flow (for instance, $W_{turb}(\Phi_0 = 0.4)/W_{turb}(\Phi_0 = 0) \simeq 0.3$, which corresponds to a reduction of turbulent energy by about 70%). This is also evident in Fig. 5, that shows the vorticity spatial field, $\nabla^2\phi$, for several of the simulations. Clearly, smaller vortical structures are present when comparing frames (a) ($\Phi_0 = 0$) and (b) ($\Phi_0 = 0.6$), as a result of the radial decorrelation felt by the turbulent eddies in the radial shear of the imposed flow. Corresponding to the decrease in W_{turb} for $\Phi_0 > 0.4$, transport becomes inhibited in the cross-flow direction, which steepens the local gradients (as revealed by the increasing ratios $W_P(\Phi_0 = 0.4)/W_P(\Phi_0 = 0) \simeq 8.8$, or $W_P(\Phi_0 = 1)/W_P(\Phi_0 = 0) \simeq 48$). There is also a significant oscillation observed in the time traces of energy for larger external amplitudes $\Phi_0 \geq 0.6$. The reason is that, as the cross-flow (i.e., radial) transport decreases for increasing Φ_0, the free energy in the gradients also increases, which in turn increases the turbulence until it can overcome the sheared flow. Also in response to the increase in the free energy, vortices start to become more prominent at larger flow amplitudes $\Phi_0 \geq 0.6$ (Fig. 5 (c)) since vortices can transport more material due to self-trapping[12,32]. The background energy W_P also reflects the bursts of fluctuation-induced transport corresponding to the oscillations in W_{turb}. These oscillations are reminiscent to the radial relaxation events induced by a fixed critical gradient ($\Phi_0 = 0$). With an externally driven sheared flow, the threshold is instead established by the balance between the sheared flow and the growth rates that are determined by the local gradients. When the local gradient is below this set threshold value, the sheared flow effectively reduces the turbulence. But, when the local gradient exceeds the threshold value, the turbulence relaxes the excess free energy. As a result, a similar turbulent relaxation is naturally established in a flux-driven system with an external sheared flow.

The impact of the externally-imposed radially-sheared poloidal flow on the background profile P is shown in Fig. 6, in which the time and poloidal averaged radial gradient of the background profile, $\langle\partial_x P\rangle_{y,t}$, can be seen.

The diffusion dominated profile is obtained by solving Eq. 1 for P without the advection term $\boldsymbol{u}\cdot\boldsymbol{\nabla}P$ for a constant injection rate $S_0 = 5$. The resulting average profile has an almost constant slope between source and sink, determined by S_0. For the base case (i.e., the one with $\Phi_0 = 0$), the average gradient profile (shown with down triangles) sits near marginality as previously stated. The main consequence of the externally-imposed flow is, as seen clearly in Fig. 6, to increase the average slope which becomes, on average, supermarginal, although still less than the diffusive profile, implying that a significant amount of radial transport still goes through the turbulent channel. This is a result of the combination of the inhibition of cross-flow transport carried out by the external flow and the flow-driven instability that triggers the turbulence. The external sheared flow is another source of free energy that can induce turbulence. In consequence, the slope does not increase without bound. Instead, it saturates due to the external flow-induced instability at a new level (marked in orange in Fig. 6) that corresponds to approximately $L_{P,x}^{-1} \simeq 5.5$. This **possibly corresponds to the establishment of a new balance between the turbulence driven at that value of the gradient and the action of the externally-imposed sheared flow. This value of $L_{P,x}^{-1}$ is based on the assumption that the system tends to be at a near marginal state on average due to the combination of the reduced cross-flow transport carried out by the external flow and the relaxations that are triggered by the flow-driven instability. The close to marginal state, on average, has been established in the no-flow case ($\Phi_0 = 0$).**

We have also probed the changes in the nature of transport caused by the externally-induced sheared flows by calculating the fractional exponent H, both in the radial and poloidal directions. The tracer rescaled range obtained for several of the simulations are shown in Fig. 7,

both for the radial and poloidal directions. The obtained exponents are shown, as a function of Φ_0, in Fig. 8. Similarly to the case with fixed-gradients, the region for timescales $\tau\Omega_i < 1$ represents the self-correlation of transport events, and is thus not interesting for long-term dynamics. For $\tau\Omega_i \gg 1$, one can see that the superdiffusive radial transport characteristic of the no-flow case ($\Phi_0 = 0$) transitions to subdiffusive at finite flow intensities. It is interesting to see that, for all intensities, the value of the exponent is very similar and around $H(v_x) \sim 0.4$. This suggests that the overall radial transport dynamics are relatively insensitive to the establishment of the limiting gradient imposed through the external sheared flow, as we discussed previously (Fig. 9). Similarly, the mildly subdiffusive poloidal transport of the no-flow case becomes strongly superdiffusive. Again, the **non-stationarity of the tracer velocities that gives an average of $H > 1$ is due to the presence** of long-lived eddies generated by the flow-driven instability. However, the deviation is less than the fixed-gradient set up since the instability can trigger relaxations in the profile, which, in turn, decreases the free energy in the gradient. **The threshold value of Φ_0 for this flux-driven setup and this flow profile has not been documented due to the dependence on the time-dependent local gradients. The competition between relaxation events and the self-generated sheared flows already present a complex interplay, and the addition of an external flow profile further convolutes the conventional interpretation of threshold values. Hence, the focus is on the change in the transport rather than the modifications on the linear stability due to the externally imposed flow profile.**
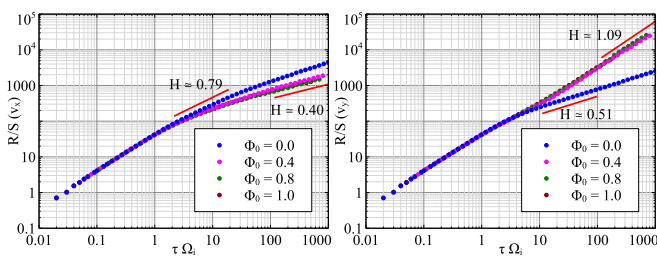
FIG. 7. Transport exponents with varying external flow amplitude Φ_0 with a flux-driven background profile also show subdiffusion in the cross-flow direction but superdiffusion in the poloidal direction. **A non-zero external flow immediately inhibits the radial transport.**

We show a last glimpse into the change in the radial dynamics caused by the externally-imposed flow by looking at the evolution of the poloidal averaged radial flux $\langle\Gamma_{P,x}\rangle_y$, that can be calculated using $\Gamma_{P,x} = Pv_x = -P\partial_y\phi$ where $P > 0$ always (thus, the sign of the flux follows that of the flow). Fig. 9 shows the temporal evolution of these fluxes for increasing external flow amplitudes, from $\Phi_0 = 0$ (frame (a)), to $\Phi_0 = 1$ (frame
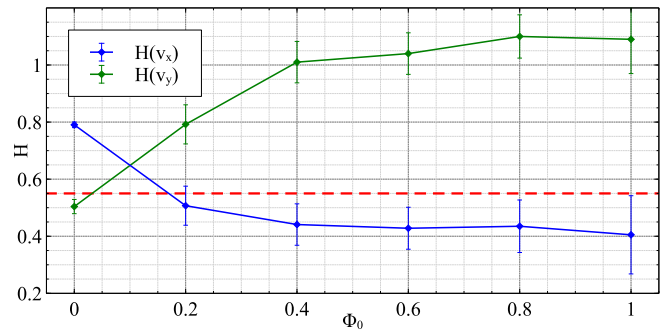
FIG. 8. Transport exponents with varying external flow amplitude Φ_0 with a flux-driven background profile also show subdiffusion in the cross-flow direction but superdiffusion in the poloidal direction. Dashed red line denotes the diffusive limit for R/S analysis.

(d)). In the no-flow case, diagonal features are apparent that reflect the ongoing coherent transport events (i.e., avalanches) that propagate down (and sometimes up) the near-marginal gradient, reminiscent of what one observes in critical-threshold sandpile models[8]. When the externally-imposed flow is present, correlated transport events still occur but are increasingly more scarce. Diagonal features in $\langle\Gamma_{P,x}\rangle_y$ are now interspersed without correlated events. This shows the impact of an external sheared flow on the cross-flow transport. Corresponding to the reduction in correlated flux events, the $\langle\partial_x P\rangle_{y,t}$ also becomes steeper on average as shown in Fig. 6. With a larger external flow amplitude of $\Phi_0 = 0.6$, $\langle\Gamma_{P,x}\rangle_y$ now shows regions of suppressed flux with down-gradient activity lasting about $t\Omega_i \sim 100$ (Fig. 9 (c)). At $\Phi_0 = 1$ in Fig. 9 (d), the duration of flux events $\langle\Gamma_{P,x}\rangle_y$ becomes somewhat shorter than $\Phi_0 = 0.6$ to approximately $t\Omega_i \sim 50$. Down-gradient correlated flux events become relatively suppressed with larger enough external flow interspersed with bursts of correlated events. Bursts in the radial flux occur due to an additional critical gradient element naturally imposed by the external sheared flow. In this regime, the local non-zero critical gradient parameter $L_{c,P,x}^{-1} = 1$ is insufficient to decorrelate the external poloidal sheared flow. However, a new limiting gradient is established at about $L_{c,P,x}^{-1} \simeq 5.5$ that weakly induces down-gradient transport. Once $\partial_x P$ is large enough to trigger a radial transport event, correlated radial transport temporarily overcomes the imposed sheared external flow. Although the gradient steepens, the values for $\langle\Gamma_{P,x}\rangle_y$ stays about the same, which means that the total time integrated poloidal averaged flux becomes smaller. Smaller and lesser fluxes down-gradient reduces the transport from the sink to the source region with increasing Φ_0.
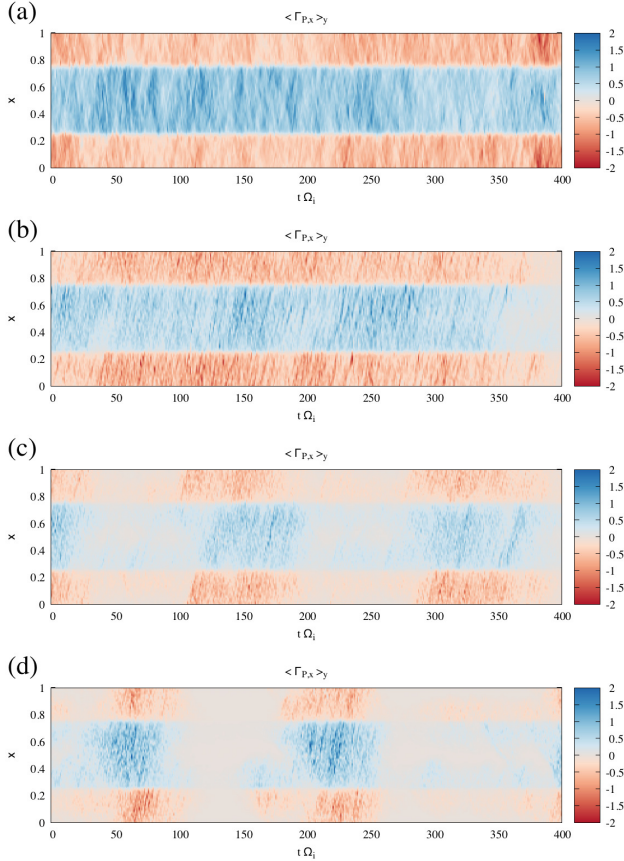
FIG. 9. Poloidal averaged radial flux $\langle\Gamma_{P,x}\rangle_y$ with increasing values of the external flow amplitude Φ_0: (a) $\Phi_0 = 0$, (b) $\Phi_0 = 0.4$, (c) $\Phi_0 = 0.6$, and (d) $\Phi_0 = 1$. Increasing Φ_0 suppresses $\langle\Gamma_{P,x}\rangle_y$ for $\Phi_0 < 0.6$ and becomes less frequent.

VI. CONCLUSIONS

In this work, we have explored the possibility of using externally-induced radially-sheared poloidal flows to tune the dynamics of radial turbulent transport in realistic, flux-driven conditions. Several lessons have been learnt. **First, externally-imposed flows readily decorrelate radial transport events and, under the proper conditions, could make the nature of transport across them diffusive or subdiffusive, even in cases of near-marginal turbulence that drive strong superdiffusive transport.** The ability to use these flows, however, has been shown to be limited by the triggering of flow-driven instabilities, of the Kelvin-Helmholtz type, that are excited when the radial shear in the flow becomes too large. The appearance of these instabilities does not impede, however, the reaching of a steady-state in which radial transport retains its subdiffusive character.

In addition, the analysis presented here illustrates the fact, once more, that the proper study of turbulent transport in near-marginal conditions necessitates of a proper evolution of background profiles simultaneously with the

turbulence, and of a wider framework to describe the overall transport dynamics that goes beyond the usual diffusive paradigm.

[1] P. W. Terry, Rev. Mod. Phys. **72**, 109 (2000).
[2] P. H. Diamond, S.-I. Itoh, K. Itoh, and T. S. Hahm, Plasma Phys. and Control. Fusion **47**, R35 (2005).
[3] U. Stroth, P. Manz, and M. Ramisch, Plasma Phys. Control. Fusion **53**, 024006 (2011).
[4] R. Sánchez, D. E. Newman, J.-N. Leboeuf, V. K. Decyk, and B. A. Carreras, Phys. Rev. Lett. **101**, 205002 (2008).
[5] R. Sánchez, D. E. Newman, J.-N. Leboeuf, and V. K. Decyk, Plasma Phys. Control. Fusion **53**, 074018 (2011).
[6] P. Diamond and T. Hahm, Phys. Plasmas **2**, 3640 (1995).
[7] B. A. Carreras, D. Newman, V. E. Lynch, and P. H. Diamond, Phys. Plasmas **3**, 2903 (1996).
[8] D. E. Newman, B. A. Carreras, and P. H. Diamond, Phys. Lett. A **218**, 58 (1996).
[9] R. Sánchez and D. E. Newman, Plasma Phys. Control. Fusion **57**, 123002 (2015).
[10] D. Ogata, D. Newman, and R. Sánchez, Phys. Plasmas (in press) (2017).
[11] R. Sánchez, B. A. Carreras, D. E. Newman, V. E. Lynch, and B. P. van Milligen, Phys. Rev. E **74**, 016305 (2006).
[12] W. Horton, Rev. Mod. Phys. **71**, 735 (1999).
[13] D. E. Newman, P. W. Terry, P. H. Diamond, and Y. Liang, Phys. Fluids B **5**, 1140 (1993).
[14] W. Horton, Phys. Fluids **29**, 1491 (1986).
[15] Y. Liang, P. H. Diamond, X. Wang, D. E. Newman, and P. W. Terry, Phys. Fluids B **5**, 1128 (1993).
[16] D. E. Newman, P. W. Terry, P. H. Diamond, Y. Liang, G. G. Craddock, A. E. Koniges, and J. A. Crottinger, Phys. Plasmas **1**, 1592 (1994).
[17] R. Numata, R. Ball, and R. L. Dewar, Phys. Plasmas **14**, 102312 (2007), 10.1063/1.2796106.
[18] J. M. Dewhurst, B. Hnat, and R. O. Dendy, Plasma Phys. Control. Fusion **52**, 025004 (2010).
[19] A. V. Pushkarev, W. J. T. Bos, and S. V. Nazarenko, Physics of Plasmas **20**, 042304 (2013).
[20] P. H. Diamond, Y.-M. Liang, B. A. Carreras, and P. W. Terry, Phys. Rev. Lett. **72**, 2565 (1994).
[21] V. Naulin, K. H. Spatschek, S. Musher, and L. I. Piterbarg, Phys. Plasmas **2**, 2640 (1995).
[22] A. C. Hindmarsh, P. N. Brown, K. E. Grant, S. L. Lee, R. Serban, D. E. Shumaker, and C. S. Woodward, ACM Trans. Math. Softw. **31**, 363 (2005).
[23] R. Metzler and J. Klafter, Phys. Reports **339**, 1 (2000).
[24] G. Zaslavsky, Phys. Rep. **371**, 461 (2002).
[25] I. Podlubny, *Fractional Differential Equations* (Academic Press, San Diego, CA, 1999).
[26] R. Sánchez, B. A. Carreras, and B. P. van Milligen, Phys. Rev. E **71**, 011111 (2005).
[27] I. Calvo, R. Sánchez, and B. A. Carreras, J. Phys. A: Math. Theor. **42**, 055003 (2009).
[28] H. E. Hurst, Trans. Amer. Soc. Civil Eng. **116**, 770 (1951).

[29] B. A. Carreras, B. P. van Milligen, M. A. Pedrosa, R. Balbín, C. Hidalgo, D. E. Newman, E. Sánchez, M. Frances, I. García-Cortés, J. Bleuel, M. Endler, C. Riccardi, S. Davies, G. F. Matthews, E. Martines, V. Antoni, A. Latten, and T. Klinger, Phys. Plasmas **5**, 3632 (1998).

[30] V. Naulin and K. H. Spatschek, Phys. Rev. E **55**, 5883 (1997).

[31] G. Manfredi and R. O. Dendy, Phys. Plasmas **4**, 628 (1997).

[32] V. Naulin, A. H. Nielsen, and J. J. Rasmussen, Physics of Plasmas **6**, 4575 (1999).

[33] S. V. Annibaldi, G. Manfredi, R. O. Dendy, and L. O. Drury, Plasma Phys. Control. Fusion **42**, L13 (2000).

[34] R. Basu, T. Jessen, V. Naulin, and J. J. Rasmussen, Phys. Plasmas **10**, 2696 (2003).

[35] S. Chandrasekhar, *Hydrodynamic and Hydromagnetic Stability* (Oxford University Press, 1961).

[36] W. Horton, T. Tajima, and T. Kamimura, Phys. Fluids **30**, 3485 (1987).

[37] T. Tajima, W. Horton, P. J. Morrison, J. Schutkeker, T. Kamimura, K. Mima, and Y. Abe, Phys. Fluids B **3**, 938 (1991).